Global sensitivity analyses of multiple conceptual models with uncertain parameters driving groundwater flow in a regional-scale sedimentary aquifer

Emanuela Bianchi Janetti[(1)], Laura Guadagnini*[(1)], Monica Riva[(1, 2)], Alberto Guadagnini[(1, 2)]

[(1)] Dipartimento di Ingegneria Civile e Ambientale (DICA), Politecnico di Milano, Piazza Leonardo da Vinci 32, 20133 Milano, Italy

[(2)] Department of Hydrology and Atmospheric Sciences, University of Arizona, Tucson, AZ, 85721, USA

* Corresponding author. Tel. +390223996263 Fax. +390223996298

E-mail address: laura.guadagnini@polimi.it

Keywords: Groundwater flow; Conceptual model uncertainty; Parameter Uncertainty; Global Sensitivity Analysis; Hydrogeological reconstruction.

Highlights:

- Comparison of Global Sensitivity Analysis (GSA) approaches in a large-scale aquifer
- Impacts of uncertain parameters of diverse conceptual models are evaluated via GSA
- Moment-based indices inform how parameters influence statistics of model outputs

Abstract

We rely on various Global Sensitivity Analysis (GSA) approaches to detect the way uncertain parameters linked to diverse conceptual geological models influence spatial distributions of hydraulic heads in a three-dimensional complex groundwater system. We showcase our analyses by considering a highly heterogeneous, large scale aquifer system located in Northern Italy. Groundwater flow is simulated considering alternative conceptual models employed to reconstruct the spatial arrangement of the geomaterials forming the internal makeup of the domain and characterizing the distribution of hydraulic conductivities. For each conceptual model, uncertain factors include the values of hydraulic conductivity associated with the geomaterials composing the aquifer as well as the system boundary conditions. We explore the relative influence of parametric uncertainties to steady-state hydraulic head distributions across the set of conceptual models considered by way of three GSA methodologies, i.e., (*a*) a derivative-based approach, which rests on the Morris indices; (*b*) the classical variance-based approach, grounded on the evaluation of the Sobol' indices; and (*c*) a moment-based GSA, which takes into account the influence of uncertain parameters on multiple (statistical) moments of a given model output. Due to computational costs, Sobol' and moment-based indices are obtained numerically through the use of a model-order reduction technique based on the polynomial chaos expansion approach. We find that the sensitivity measures considered convey different yet complementary information. The choice of the conceptual model employed to characterize the lithological reconstruction of the aquifer affects the degree of influence that uncertain parameters can have on modeling results.

1. INTRODUCTION

Modeling flow and transport processes in complex aquifers is prone to uncertainty, due the (unknown) spatial distribution of medium properties (e.g., hydraulic conductivity) and the conceptual and mathematical model adopted to describe the behavior of the system. Global Sensitivity Analysis, GSA, is a powerful tool to enable quantification of the influence of uncertain model inputs on an output of interest, y (Razavi and Gupta, 2015; Song et al., 2015; Pianosi et al., 2016, and references therein). As compared to local sensitivity analysis (Saltelli et al., 2005), GSA measures the relative contribution of uncertain model factors (as well as their combined effects) to a global metric representing the variability of model output y. Common purposes of GSA techniques comprise (*i*) screening of model parameters, i.e., identification of input variables having limited influence on y; (*ii*) ranking of model parameters, i.e., ordering model input parameters according to their relative influence on y; and (*iii*) providing information to drive probabilistic risk analyses and/or parameter estimation through model calibration.

A variety of approaches has been proposed to perform GSA. These comprise derivative-based (Morris, 1991; Malaguerra et al., 2013; Campolongo et al., 2007), variance-based (Sobol, 1993, 2001; Sudret, 2008; Fajraoui et al., 2011; Sochala and Le Maître, 2013), regression-based (Box and Draper, 1987; Sudret, 2008) and moment-independent (Borgonovo et al., 2011; Pianosi and Wagener, 2015) techniques. Dell'Oca et al. (2017) proposed a moment-based approach to GSA. These authors rely on new metrics, termed AMA indices, that quantify the relative contribution of each uncertain model parameter to the main features (as rendered by the statistical moments) of the probability density function of model output y. One of their main findings is that relying on classical variance-based GSA methods, with the implicit assumption that the uncertainty of y is fully characterized by its variance, can lead at best to an incomplete picture of the system response to model parameter uncertainties. The proposed methodology is illustrated by Dell'Oca et al. (2017) and Maina and Guadagnini (2018) on relatively simple test cases.

Local and global (mainly variance-based) sensitivity analyses have been performed to assess the degree of influence of uncertain parameters on groundwater flow and transport models at the field/regional scale (Laloy et al., 2013; Rajabi et al., 2015; Deman et al., 2015; Kerrou et al., 2017; Rajabi and Ketabchi, 2017; Chen et al., 2018). All of these studies consider the presence of a unique conceptual/mathematical model describing the behavior of the system. Dai et al. (2017) apply a variance-based GSA approach to assess the relationship between uncertainties arising from several alternative conceptual models and their corresponding input parameters and boundary conditions.

An exhaustive analysis of the ability, efficiency and practical applicability of diverse GSA procedures to identify the most relevant inputs in complex heterogeneous three-dimensional systems whose hydrogeological make-up is reconstructed through differing conceptual modeling strategies is still lacking. This is precisely the objective of this study. We do so by comparing sensitivity analysis results obtained through (*a*) a derivative-based approach, grounded on the widely used Morris indices; (*b*) the classical variance-based approach which rests on the evaluation of the Sobol' indices; and (*c*) the novel moment-based GSA of Dell'Oca et al. (2017), which can provide information on multiple statistics of the probability distribution of the output variable of interest. As a test bed, we consider a large scale aquifer system located in Northern Italy (see Section 2). The area is highly heterogeneous and is characterized by the presence of high-quality water springs interacting with the groundwater system. The spatial distribution of geomaterials forming the internal makeup of the subsurface and of the associated hydraulic attributes, as well as boundary conditions are highly uncertain. In this context, we investigate the way the joint analysis of multiple GSA metrics can contribute to ranking the importance of uncertain factors of multiple origins on the response of the aquifer system, as given by the steady-state distribution of hydraulic heads. As an additional distinctive element, we also explore the way parametric uncertainties are influential to hydraulic head distributions across the set of alternative conceptual models that can be employed to characterize the lithological reconstruction of the aquifer (and ultimately the spatial distribution of aquifer hydraulic conductivity).

2. STUDY AREA

The study area (see Fig. 1) is part of the high-medium Alluvial Po Plain in Northern Italy and encompasses a planar surface of about 785 km^2. It is located in the area comprised between the two main rivers (Adda and Serio) in the region and hosts activities linked to agricultural (84%) and urban (16%) sectors. A main feature of the area is the presence of high-quality water springs. These natural springs are key environmental drivers and constitute treasures around which local economies thrive, forming a unique ecosystem with remarkable appeal for tourism and leisure activities. They also constitute the main water supply for agriculture, which is an important anthropogenic activity in the area. Figure 1b depicts the major hydrogeological features of the area, together with the general pattern of the ground surface elevation and the location of the springs.

Groundwater resources within the Po plain are mostly located in the continental and marine layers of Plio-Pleistocene age. The quaternary sedimentary sequence is overall regressive and is formed by (from bottom to top) (*i*) basal turbiditic sands and clays, (*ii*) a prograding fluvio-deltaic sedimentary wedge, and (*iii*) continental sediments (Regione Emilia-Romagna, ENI-AGIP, 1998; Regione Lombardia, ENI-AGIP, 2002). In Section 3 we propose three alternative models for the reconstruction of the hydrogeological architecture of the study area on the basis of geological-stratigraphic data collected at 189 locations (available at http://www.geoportale.regione.lombardia.it/download-dati) and hydro-geological sections available from previous studies (Maione et al., 1991; Beretta et al., 1992; Regione Lombardia, ENI-AGIP, 2002). As an example, Figure 2 depicts a North-South (SECT 1) and an East-West (SECT 2) vertical cross-section whose planar location is indicated in Fig. 1. The system has an average thickness of about 120 m (with stratigraphic data available up to a depth of about 300 m in some areas) and comprises a surface (locally semi-confined) and a deep (confined-semiconfined) aquifer. The surface aquifer has a thickness of about 60 m and is mainly formed by compact/fractured conglomerate (fluvio-glacial Mindel) deposits in the Northern area and by fluvio-glacial gravels and sands (Riss-Wurm) intercalated by lenses of clay with variable planar/lateral extent in the Southern zone. The deep aquifer is formed by alternating coarse clastic (fractured conglomerates in the Northern area) sediments and clays whose degree of continuity and relative thickness vary in space. In the median portion of the plain, the thickness of the modeled system is characterized by a significant reduction controlled by the subsurface geological structure (e.g., Maione et al., 1991).

Additional available data include: precipitation and temperature collected at 5 meteorological stations, rivers' water level monitored at 3 hydrometric stations, as well as pumping rates and piezometric levels recorded at 120 pumping/monitoring wells (see Fig. 1b). Average groundwater flow is from North to South, the Adda river generally draining water from the aquifers and the Serio river recharging and draining the aquifer in the Northern and Southern sectors, respectively.

3. METHODOLOGY

3.1 Spatial distribution of Geomaterials and associated hydraulic conductivities

The analysis of available sedimentological information allows identifying a set of n_f = 5 main geomaterials (facies/classes) which constitute the geological makeup of the system. Each geomaterial, denoted as M_i (i = 1, ..., 5), is listed in Table 1 together with the corresponding volumetric fraction, f_i, encountered within the study area. The experimental directional (indicator) variogram, $\gamma_\alpha^i\left(s_\alpha\right)$ (s_α being spatial separation distance, $\alpha = h$, or v

indicating horizontal or vertical direction, respectively) has been evaluated for each facies and interpreted through a maximum likelihood (ML) approach with an exponential model, i.e., $\gamma_\alpha^i(s_\alpha) = \sigma^i\left[1-\exp\left(-3s_\alpha/r_\alpha^i\right)\right]$, σ^i and r_α^i respectively representing variogram sill and directional range of sedimentological class *i*. ML estimates of the variogram sill σ^i (not shown) virtually coincide with their theoretical counterparts $f_i(1-f_i)$. ML estimates ($\hat{r}_\alpha^i$) of r_α^i are listed in Table 1 for all facies. The degree of correlation along the horizontal direction, as quantified by $\hat{r}_h^i$, attains its largest values for classes 3 and 4, suggesting the occurrence of horizontally elongated features where gravel and compact conglomerates are dominant. Class 4 and 5 are highly correlated along the vertical direction, showing that the compact and fractured conglomerates tend to form relatively thick layers.

To reconstruct the three-dimensional distribution of geomaterials, we discretize the aquifer system of extent 23 km (East-West direction) × 48 km (North-South direction) × 475 m (depth) through blocks of uniform size 100 m × 200 m × 5 m, according to the information and computational resources available, for a total of N_C = 5.2 millions voxels. Conditional Indicator Kriging (e.g., Isaaks and Srivastava, 1990) yields n_f × N_C values of $I_{i,j}$ (with $\sum_{i=1}^{n_f} I_{i,j} = 1,\ \forall j$), corresponding to the estimated probability that a given geomaterial class M_i resides within block *j* (i.e., the volumetric percentage of M_i within block *j*).

Here, we propose a further elaboration of the multiple continua concept, hereafter called *Overlapping Continua* (*OC*) model to evaluate hydraulic conductivity at each voxel of the domain. The *OC* model is grounded on the concept that the system can be viewed as formed by a collection of media of differing properties coexisting in space. The idea is that each voxel *j* of the numerical grid represents a finite volume within which all geomaterials (or facies) can coexist, each associated with a given volumetric fraction. Hydraulic conductivity at block *j* is evaluated as a weighted mean of facies conductivities, k_i. In Section 4 we analyze the impact on hydraulic head patterns of two variants of *OC*, according to which hydraulic conductivity is computed as a weighted arithmetic ($K_j^{OC\_A}$) or geometric ($K_j^{OC\_G}$) mean of k_i as

$$K_j^{OC\_A} = \sum_{i=1}^{n_f} I_{i,j}\, k_i\,; \qquad\qquad K_j^{OC\_G} = \prod_{i=1}^{n_f} k_i^{I_{i,j}} \tag{1}$$

Outcomes of this model are compared against corresponding results obtained with a *Composite Medium* (*CM*) approach (e.g., Winter et al., 2003; Guadagnini et al., 2004 and references therein) where each block of the numerical model is considered to be formed by a single geomaterial with conductivity $K_j^{CM} = k_i$ (index *i* identifying the facies attributed to cell *j*). The spatial distribution of geomaterials is estimated according to the procedure described by Guadagnini et al. (2004) and based on conditional indicator Kriging. These authors start by considering facies M_1, assigning indicator $I = 1$ to locations where M_1 is observed and $I = 0$ otherwise. The region occupied by M_1 is delineated by imposing to the kriged field a threshold corresponding to the value of f_1, to reconstruct a spatial distribution of M_1 which is consistent with the observed volumetric fraction. This procedure is repeated for (n_f − 1) facies, progressively removing at each iteration the portion of the aquifer already assigned to a given class in the previous step.

3.2 Groundwater flow model

The widely tested numerical code MODFLOW-2005 (Harbaugh, 2005) is employed to simulate steady-state groundwater flow within the domain described in Section 3.1. Inactive cells are inserted to reconstruct the topographic surface of the area and the bottom of the system, resulting in about one million active cells. Recharge terms included in the study comprise infiltration from precipitation, irrigation and percolation from channels in the non-urban zones, or aqueduct and sewage system losses in the urban sector. Since exhaustive and up-to-date records detailing the exact location of the pumping wells are not available, for the illustration of our approach we assign the total water withdrawal within a given municipality to a system of wells located at the center of the municipality itself. Springs are simulated as drains so that their outflow-rate is proportional to the difference between hydraulic head and elevation of ground level. Dirichlet boundary conditions are set along the rivers, this choice relying on results of previous studies, showing that both rivers have a direct hydraulic connection with the groundwater system (Maione et al., 1991). Neumann boundary conditions are set along the Northern boundary of the model (see Fig. 3) on the basis of the hydrological study of the Serio basin (located North of the study area) performed by Rametta (2008), as also discussed in Session 3.3.

3.3 Sensitivity analysis

In Section 4 we analyze the impact of the uncertainty in the conceptual model (the two variants of *OC* versus *CM*), boundary conditions and hydraulic parameters on the groundwater system response, as quantified in terms of steady-state hydraulic heads obtained at a sub-set of 39 wells, whose locations are depicted in Fig. 3, covering the full investigated area. We place our GSA before model calibration. As such, each conceptual model is characterized by the same weight and the interval of variability of model parameters is possibly largest. As such, the GSA here performed is mainly keyed to (*i*) improving our understanding of the behavior of each of the candidate models, in terms of the relevance of each model parameter on the target model output, and (*ii*) identifying parameters which might be of limited influence in the context of a subsequent model calibration (e.g., Liu et al., 2006; Hutcheson and McAdams, 2010). The uncertain model inputs associated with (*a*) hydraulic conductivity values (k_i, with i = 1,…, 5) of the five geomaterials composing the subsurface, (*b*) the total flow rate entering the domain from the Northern boundary, and (*c*) the Dirichlet boundary conditions set along the rivers are collected in a N-dimensional vector $\mathbf{p}$. Entries of the latter are independent and identically distributed (i.i.d.) random variables, p_i (with i = 1,…, N; N = 7), each characterized by a uniform probability density function, pdf. This modeling choice rests on the idea of assigning equal weight to each value of the distribution. The (random) parameter space is then defined as $\mathbf{\Gamma} = \left[\mathbf{p}^{\min}, \mathbf{p}^{\max}\right]$ where $\mathbf{p}^{\min}$ and $\mathbf{p}^{\max}$ indicate vectors respectively containing lower ($p_i^{\min}$) and upper ($p_i^{\max}$) bounds of parameter variability intervals, as listed in Table 2. The choice of $p_i^{\min}$ and $p_i^{\max}$ (i = 1,…,5) is based on typical hydraulic characteristics of each geomaterial class. With reference to boundary conditions, Rametta (2008) estimated a total incoming flow rate in the area of interest equal to $\overline{p}_6$ = 9.65 m^3/s. Since this estimated value is affected by uncertainty and the spatial distribution of $\overline{p}_6$ is unknown, we consider the incoming flow rate as uniformly distributed along the Northern domain boundary and set $p_6^{\min} = 0.5 \times \overline{p}_6$ and $p_6^{\max} = 1.5 \times \overline{p}_6$ (resulting in a coefficient of variation of about 30%). The support of the Dirichlet boundary condition (p_7) has been defined considering that the river stage may vary between the river bottom and the banks' elevation.

We applied three methodologies, characterized by differing degrees of complexity, to quantify the impact of uncertainty in **p** on model-based hydraulic heads.

The Morris indices (Morris, 1991; Campolongo et al., 2007) rely on the evaluation of incremental ratios, denoted as elementary effects, and are computed for each uncertain quantity p_i along r trajectories in the parameter space $\mathbf{\Gamma}$. The elementary effect of p_i computed along trajectory m, $EE_{p_i}(m)$, is defined as

$$EE_{p_i}(m) = \frac{f(p_1, \ldots, p_i + \Delta, \ldots, p_N) - f(\mathbf{p})}{\Delta} \tag{2}$$

Here, $f(\mathbf{p})$ is the model output, and Δ is a fixed increment evaluated as described by Campolongo et al. (2007). To avoid effects of the starting point in the parameter space on the sensitivity analysis (Morris, 1991), we evaluate EE_{p_i} for r trajectories, and compute the Morris index as

$$\mu^*_{p_i} = \frac{1}{r}\sum_{j=1}^{r}\left|EE_{p_i}\left(j\right)\right| \tag{3}$$

This methodology is computationally efficient because it requires a relative low number of forward model simulations, i.e., $r\left(N+1\right)$. In our application we obtain stable results with r = 30 (i.e., 240 model runs). Note that $\mu^*_{p_i}$ cannot quantify the joint effect of uncertainty of model inputs on the uncertainty of $f\left(\mathbf{p}\right)$. This type of information can be obtained by relying on the Sobol' (Sobol, 1993, 2001; Sudret, 2008; Formaggia et al., 2013 and references therein) and AMA (Dell'Oca et al., 2017; Ceriotti et al., 2018) indices.

It can be shown (Sobol, 1993) that if the model response $f\left(\mathbf{p}\right)$ belongs to the space of square integrable functions, then the following expansion holds

$$f\left(\mathbf{p}\right) = f_0 + \sum_{i=1}^{N} f_{p_i}\left(p_i\right) + \sum_{1\le i<j\le N} f_{p_i,p_j}\left(p_i,p_j\right) + \cdots + f_{p_1,\ldots,p_N}\left(p_1,\ldots,p_N\right) \tag{4}$$

where f_0 is the expected value of $f\left(\mathbf{p}\right)$ and $f_{p_1,\ldots,p_s}\left(\left\{p_1,\ldots,p_s\right\}\subseteq\left\{1,\ldots,N\right\}\right)$ are orthogonal functions with respect to a probability measure. The total variance, $V\left[f\right]$, of $f\left(\mathbf{p}\right)$ can then be decomposed as

$$V\left[f\right] = \sum_{i=1}^{N} V_{p_i} + \sum_{1\le i<j\le N} V_{p_i,p_j} + \cdots + V_{p_1,\ldots,p_N} \tag{5}$$

where V_{p_i} is the contribution to $V\left[f\right]$ due solely to the effect of p_i, and $V_{p_1,\ldots,p_s}$ is its counterpart due to interaction of model parameters belonging to the subset $\left\{p_1,\ldots,p_s\right\}$. The Sobol' indices, S_{p_i} and $S_{p_1,\ldots,p_s}$ are defined as

$$S_{p_i} = \frac{V_{p_i}}{V\left[f\right]}; \qquad S_{p_1,\ldots,p_s} = \frac{V_{p_1,\ldots,p_s}}{V\left[f\right]} \tag{6}$$

respectively quantifying the contribution of only p_i and the joint effect of $\{p_1,...,p_s\}$ on $V\left[f\right]$. The total contribution of p_i to $V\left[f\right]$ is quantified by the total Sobol' index

$$S_{p_i}^{T} = S_{p_i} + \sum_{j} S_{p_i,p_j} + \sum_{j,k} S_{p_i,p_j,p_k} + ...+ S_{p_i,...,p_N} \tag{7}$$

The AMA indices (introduced by Dell'Oca et al., 2017) allow quantifying the expected variation of a given statistical *moment* $M\left[f\right]$ of the pdf of $f\left(\mathbf{p}\right)$ due to conditioning on parameter values. These are defined as

$$\mathrm{AMA}M_{p_i} = \begin{cases} \dfrac{1}{\left|M\left[f\right]\right|} \displaystyle\int_{\Gamma_{p_i}} \left|M\left[f\right] - M[f \mid p_i]\right| \rho_{\Gamma_{p_i}} dp_i & if\ M\left[f\right] \neq 0 \\ \displaystyle\int_{\Gamma_{p_i}} \left|M\left[f\right] - M[f \mid p_i]\right| \rho_{\Gamma_{p_i}} dp_i & if\ M\left[f\right] = 0 \end{cases} \tag{8a}$$

$$\mathrm{AMA}M_{p_1,...,p_s} = \begin{cases} \dfrac{1}{\left|M\left[f\right]\right|} \displaystyle\int_{\Gamma_{p_1,...,p_s}} \left|M\left[f\right] - M[f \mid p_1,...,p_s]\right| \rho_{\Gamma_{p_1,...,p_s}} dp_1...dp_s & if\ \ M\left[f\right] \neq 0 \\ \displaystyle\int_{\Gamma_{p_1,...,p_s}} \left|M[f \mid p_1,...,p_s]\right| \rho_{\Gamma_{p_1,...,p_s}} dp_1...dp_s & if\ \ M\left[f\right] = 0 \end{cases}$$

(8b)

Here, $\mathrm{AMA}M_{p_i}$ (8a) and $\mathrm{AMA}M_{p_1,...,p_s}$ (8b) correspond to the AMA indices associated with a given statistical moment *M* and related to variations of only p_i or considering the joint variation of $\{p_1,...,p_s\}$, respectively; $\rho_{\Gamma_{p_i}}$ is the marginal pdf of p_i, $\rho_{\Gamma_{p_1,...,p_s}}$ being the joint pdf of $\{p_1,...,p_s\}$; and $M[f \mid p_1,...,p_s]$ indicates conditioning of the (statistical) moment *M* on known values of parameters $p_1,...,p_s$. Note that $\mathrm{AMA}V_{p_i}$, i.e., the AMA index related to the variance (*M* = *V*) of $f\left(\mathbf{p}\right)$, coincides with the principal Sobol' index S_{p_i} only if the conditional variance, $V[f \mid p_i]$ is always (i.e., for each value of p_i) smaller than (or equal to) its unconditional counterpart $V\left[f\right]$. If $V[f \mid p_i]$ can undertake values that are larger than

$V[f]$ while varying p_i, then $\mathrm{AMA}V_{p_i} > S_{p_i}$. Note also that, in this latter case, $\mathrm{AMA}V_{p_i}$ can be either smaller or larger than $S_{p_i}^T$, depending on the relative impact of the interaction terms $f_{p_1,\ldots,p_s}$. In Section 4 we further analyze the difference amongst $\mathrm{AMA}V_{p_i}$ and the Sobol' indices by means of the considered test scenario.

The numerical evaluation of Sobol' and AMA indices can be time consuming and can become unfeasible in complex settings, such as the one here assessed. These metrics are evaluated in Section 4 relying on a surrogate model based on the generalized Polynomial Chaos Expansion (gPCE) (Ghanem and Spanos, 1991; Xiu and Karniadakis, 2002; Le Maître and Knio, 2010). This technique consists in approximating $f(\mathbf{p})$ by a linear combination of multivariate orthonormal Legendre polynomials, i.e., $\psi_{\boldsymbol{x}}(\boldsymbol{p})$

$$\begin{aligned} & f(\boldsymbol{p}) \cong f_0 + \sum_{i=1}^{N} \sum_{\boldsymbol{x} \in \Im_i} \beta_{\boldsymbol{x}} \psi_{\boldsymbol{x}}(\boldsymbol{p}) + \sum_{i=1}^{N} \sum_{j>i}^{N} \sum_{\boldsymbol{x} \in \Im_{i,j}} \beta_{\boldsymbol{x}} \psi_{\boldsymbol{x}}(\boldsymbol{p}) + \ldots; \\ & \psi_{\boldsymbol{x}}(\boldsymbol{p}) = \prod_{i=1}^{N_p} \psi_{i,x_i}(p_i); \quad \beta_{\boldsymbol{x}} = \int_{\Gamma} f(\boldsymbol{p}) \psi_{\boldsymbol{x}}(\boldsymbol{p}) \rho_{\Gamma \boldsymbol{p}} \, d\boldsymbol{p}, \end{aligned} \tag{9}$$

where $\boldsymbol{x} = \{x_1, \ldots, x_N\} \in \mathrm{N}^N$ is a multi-index expressing the degree of each univariate polynomial, $\psi_{i,x_i}(p_i)$; $\beta_{\boldsymbol{x}}$ are the gPCE coefficients; $\rho_{\Gamma \boldsymbol{p}}$ is the pdf of $\mathbf{p}$; $\Im_i$ contains all indices such that only the i-th component does not vanish; $\Im_{i,j}$ contains all indices such that only the i-th and j-th components are not zero, and so on.

Coefficients $\beta_{\boldsymbol{x}}$ in Eq. (9) are calculated through an approach based on a regression method (Sudret, 2008). The latter requires evaluating the full model and its gPCE approximation at a number of points in the parameter space, $\boldsymbol{\Gamma}$, and then minimizing the sum of the square of the differences between these two solutions. Here, accurate results have been obtained truncating the gPCE at order 4 (not shown), requiring 2437 simulations performed using a quasi- Monte Carlo sampling technique (see e.g., Feil et al., 2009; Fajraoui et al., 2012;

Maina and Guadagnini, 2018, and references therein). In this study we use Legendre polynomials in Eq. (9). These are orthonormal with respect to the uniform pdf $\rho_{\Gamma_{\boldsymbol{p}}} = \prod_{i=1}^{N} \left(p_i^{\max} - p_i^{\min} \right)^{-1}$. Note that, if prior information on uncertain parameters are available, the approach can still be employed upon relying on different parameter distributions. For instance, Jacobi and Hermite polynomials are associated with beta and Gaussian pdfs, respectively (Xiu and Karniadakis, 2002; Sudret, 2008).

4. RESULTS AND DISCUSSION

As an example of the main features of the conductivity fields obtained with the three conceptual models described in Section 3, Fig. 4 depicts the spatial distribution of the natural logarithm of hydraulic conductivity, *Y*, along a longitudinal cross section obtained by setting k_1 = 10^{-7} m/s, k_2 = 10^{-6} m/s, k_3 = 10^{-3} m/s, k_4 = 10^{-5} m/s, and k_5 = 10^{-2} m/s, corresponding to the mean values of $\log k_i$ associated with the intervals of variability listed in Table 2.

As already discussed in Section 3, in *CM* (Fig. 4a) only one geomaterial resides in each cell. Therefore, this modeling concept may lead to the occurrence of blocks characterized by very different *Y* values that can be close (or contiguous) across the system. The adoption of *OC* leads to a smoother spatial distribution of *Y*. We further note that the two diverse averaging strategies described in Section 3.1 can significantly affect the spatial distribution of *Y*. The domain is (on average) more permeable and less heterogeneous when the arithmetic rather than the geometric mean operator is employed. This aspect is further elucidated by Fig. 5 where the sample pdfs of $Y^{OC\_A} = \ln K^{OC\_A}$ and $Y^{OC\_G} = \ln K^{OC\_G}$ (corresponding to the fields related to the cross-sections depicted in Figs. 4b and 4c, respectively) are plotted in natural (Fig. 5a) and semi logarithmic (Fig. 5b) scale. Also shown for comparison are (*i*) Gaussian distributions having the same mean and variance as the sample pdfs and (*ii*) the sample pdf of *Y* evaluated for *CM* (and related to the field linked to the cross-section in Fig. 4a). As expected, the mean of Y^{OC_A} is larger than the mean of Y^{OC_G}, because the arithmetic mean operator tends to assign increased weight to large k_i values as compared to the geometric mean operator. We note that Y^{OC_G} values are associated with a larger variance than their Y^{OC_A} counterparts. This notwithstanding, the tails of the Y^{OC_G} distribution decay following a (nearly) Gaussian pdf, while the distribution of Y^{OC_A} displays a long left tail. In other words, even as the Y^{OC_A} field is (overall) less heterogeneous than Y^{OC_G}, it is characterized by a significant occurrence of low values.

Figure 6 depicts (*i*) the Morris indices $\mu^*_{p_i}$ (Fig. 6a); (*ii*) the normalized Morris indices (Fig. 6b), defined as $\bar{\mu}^*_{p_i} = \mu^*_{p_i} \Big/ \sum_{i=1}^{N} \mu^*_{p_i}$; (*iii*) the principal, S_{p_i} (Fig. 6c) and total, $S^T_{p_i}$ (Fig. 6d), Sobol' indices, as well as (*v*) the AMA indices linked to the mean, $\text{AMA}E_{p_i}$ (Fig. 6e), variance, $\text{AMA}V_{p_i}$ (Fig. 6f), and skewness, $\text{AMA}\gamma_{p_i}$ (Fig. 6g), computed at all 39 target locations for *CM* and considering all seven uncertain model inputs p_i. Note that each well is associated with an Identification Number (ID) that increases from North to South to facilitate the interpretation of the results (see also Fig. 3). Corresponding results for settings associated with the *OC* modeling strategies (termed as *OC_A* and *OC_G*, when considering the arithmetic or geometric averaging operator, respectively) are depicted in Figs. 7 and 8.

The diverse GSA metrics considered yield different yet complementary information.

For all conceptual models, $\mu^*_{p_i}$ and $\text{AMA}E_{p_i}$ tend to decrease from North to South, suggesting that the mean behavior of the groundwater levels is more affected by uncertainty in model parameters in the Northern than in the Southern investigated area. Values of $\text{AMA}E_{p_i}$, quantifying the impact (on average) of uncertain inputs on hydraulic heads are in general quite low for *OC_A* and *CM* while they can be significant (> 20%) for *OC_G*.

All considered indices indicate that k_2 and k_4 have a limited (and in some cases negligible, as further discussed below) influence in any of the conceptual models analyzed. This result is consistent with the observation that these parameters correspond to geomaterials that respectively constitute only about 5% and 15% of the system and are characterized by intermediate conductivity values. Otherwise, k_3 and k_5, which are linked to the most permeable facies, affect all metrics computed in most observation points even as facies 5 constitutes only about 10% of the domain. In particular, amongst facies conductivities, k_5 is identified as the most relevant parameter for *OC_A*, k_3 being most influential for *OC_G* and *CM*. Moreover, uncertainty associated with k_1, corresponding to the less permeable facies, significantly affects model outcomes for *OC_G* and *CM* while its effect is negligible in *OC_A*, despite the high volumetric percentage (≈ 37%) of facies 1. All these results are consistent with the conceptual models adopted, *OC_A* being conducive to a reduction of the importance of the low conductivity facies while enhancing the effect of highly permeable textures. The effect of the Adda and Serio river stage (as embedded in p_7) increases from North to South and is particularly significant for *OC_A*. Boundary conditions at the Northern boundary (as embedded in p_6) affect mainly the Northern sector of the domain for *OC_A*, their influence extending also within the Southern sector for *OC_G*. The latter result is associated with the combined effects of the model boundary conditions and the tendency of *OC_G* to be overall characterized by relatively low *Y* values that enhance hydraulic head variations due to inflow changes. With reference to *CM*, the impact of p_6 on model outputs significantly varies with the considered metrics. This aspect is investigated in the following.

As highlighted above, albeit traditional (Morris and Sobol') and AMA indices provide overall similar results, outcomes of the diverse metrics not always appear to be mutually consistent. For example, considering *CM* one can see that while the analysis of S_{p_i} (Fig. 6c) would suggest a negligible impact of k_2 and a very limited impact of k_4 and p_6 on model outputs localized in the Northern area of the system, indices $S_{p_i}^T$, AMAV_{p_i} and AMAγ_{p_i} (Figs. 6d, f, g) suggest that the impact of k_2, k_4, p_6 is (albeit to a limited extent for k_2 and k_4) not negligible in most of the considered target locations. A qualitatively similar observation can be made for model *OC_G* with reference to parameters k_2 and k_4 (compare Fig. 8c and Figs. 8d, f, g).

In order to explain this behavior, we recall that Sobol' and AMAV_{p_i} indices are based on diverse perspectives. Principal, S_{p_i}, and total, $S_{p_i}^T$, Sobol' indices rely on the decomposition of the output variance, $V\left[f\right]$, as given by Eq. (5) and allow quantifying the expected reduction of $V\left[f\right]$ due the knowledge of p_i. The AMAV_{p_i} metric evaluates (on average) the distance between $V\left[f\right]$ and the variance conditional to the knowledge of p_i, i.e., $V[f \mid p_i]$. Therefore, differences among S_{p_i}, $S_{p_i}^T$ and AMAV_{p_i} are mostly related to the behavior of the conditional variance $V\left[f|p_i\right]$, as we already mention in Section 3.3. As an example, Figs. 9a-c depicts the conditional variance $V\left[f|p_i\right]$ versus p_i at a selected observation well (ID 32), together with its unconditional counterpart. Here, the interval of variation of each model parameter has been normalized to span the range [0, 1] for graphical representation purposes. Conditional moments are obtained via 2×10^6 runs of the gPCE-based surrogate model. We note that $V\left[f|k_2\right]$, $V\left[f|k_4\right]$ and $V\left[f|p_6\right]$ for *CM* (Fig. 9a) can be either smaller or higher than their unconditional counterparts, depending on the conditioning value p_i. This behavior is consistent with inability of the principal Sobol' index to detect the effect of k_2, k_4 and p_6 on the model output variance at this observation well (see Fig. 6c), integration of the conditional variance over k_2, k_4 and p_6 being close to zero. A similar conclusion can be drawn from Figs. 8c,f and

Fig. 9c, with reference to parameters k_2 and k_4 for model *OC_G*. Conversely, $V\left[f\left|k_3\right.\right] < V\left[f\right]$ for most (or all) values of k_3 in both *CM* and *OC_G* models. Thus, S_{k_3} and $\mathrm{AMA}V_{k_3}$ yield very similar results. For the same reason S_{p_i} (Fig. 7c) and $\mathrm{AMA}V_{p_i}$ (Fig. 7f) exhibit very consistent features for *OC_A*, identifying k_5 and p_7 as the most influential parameters, $V\left[f\left|k_5\right.\right]$ and $V\left[f\left|p_7\right.\right]$ being always smaller than the unconditional variance, as revealed by Fig. 9b.

The impact of the interaction among parameters on the total output variance, as identified by the total Sobol' and AMA*V* indices and corresponding to settings where $S_{p_i}^T > S_{p_i}$, $\mathrm{AMA}V_{p_i}$ $> S_{p_i}$ and $\sum_{i=1}^{N} S_{p_i}^T > 1$, is in our case mainly relevant for *CM* and *OC_G* in the Southern area (see Figs. 6d and 8d), while being generally limited for *OC_A* where it is detectable only at a few target points in the Northern zone (see Fig. 7d). The scatterplot of $S_{p_i}^T$ versus S_{p_i} is depicted in Figs. 10a-c for all target points, parameters and models investigated. Interactions are mostly detected for k_3 and k_5 for all models. Scatterplots of $\mathrm{AMA}V_{p_i}$ versus $S_{p_i}^T$ (Figs. 10 d-f) reveal that $S_{p_i}^T$ can be smaller or larger than $\mathrm{AMA}V_{p_i}$, depending on the target point and parameter considered. This latter behavior is associated with the relative impact of the interaction terms that can vary for differing model conceptualizations and from one target point to another.

The degree of symmetry of the pdfs of hydraulic heads, as driven by the skewness, strongly depends on the considered conceptual model and on the selected observation well. In most of the observation wells the unconditional pdf is right-skewed for *CM* and *OC_G* while being left-skewed or symmetric for *OC_A* (not shown). As an example, the unconditional and conditional skewness obtained for the three considered models are depicted in Fig. 9d-f at observation well (ID 32). Conditioning on model parameters affects the shape of the pdf, whose degree of symmetry can markedly depend on the conditioning value of p_i.

In order to provide an overall assessment of model parameter impacts on hydraulic heads across the domain, we compute the average of each sensitivity index across all 39 locations considered (the averaging operator is hereafter denoted with symbol $\langle\ \rangle$). Figure 11a depicts $\langle S^T_{p_i} \rangle$ versus $\langle \bar{\mu}^*_{p_i} \rangle$ for all model conceptualizations analyzed. These two traditional sensitivity measures display the following consistent trends (only a few minor differences in term of ranking of parameter importance can be detected): (*i*) hydraulic head for all conceptual models are significantly affected by the uncertainty of k_3 and k_5, while the effects of k_2 and k_4 are negligible; (*ii*) the strength of the influence of the uncertainty of k_1 depends on the conceptual geological model adopted, in particular it is negligible in *OC_A*; (*iii*) *CM* and *OC_A* are more affected by the uncertainty in the Dirichlet (as quantified by p_7) than in the Neumann (i.e., p_6) boundary condition, the opposite behavior being observed for *OC_G*.

The scatterplot of $\langle \mathrm{AMA}V_{p_i} \rangle$ versus $\langle \mathrm{AMA}E_{p_i} \rangle$ values is depicted in Fig. 11b. We note that mean values of hydraulic heads in *OC_G* are more affected by uncertainty in a few selected parameters (k_1, k_3, k_5, and p_6) with respect to what can be observed for the other models (note the isolated cluster of green symbols, i.e., diamonds, in Fig. 10b). Conversely, hydraulic head variance is influenced (on average) in a similar way for all considered models by the input parameters which are evaluated as most influential (i.e., k_3 for *CM* and *OC_G*; and k_5 and p_7 for *OC_A*). Comparing $\langle \mathrm{AMA}V_{p_i} \rangle$ and $\langle S^T_{p_i} \rangle$ (Fig. 11c) enables us to further support our previous observation that both sensitivity measures are able to identify interactions among parameters, albeit in a different way. Interactions are generally limited for *OC_A*, these two averaged metrics displaying a linear trend with unit slope. For *CM* and *OC_G*, where interaction terms are more relevant, $\langle \mathrm{AMA}V_{p_i} \rangle$ tends to be slightly higher than $\langle S_{p_i}^{T} \rangle$ for all input parameters, with the exception of k_3.

Figure 10d depicts $\langle \mathrm{AMA}V_{p_i} \rangle$ versus $\langle \mathrm{AMA}\gamma_{p_i} \rangle$. We note that all points tend to follow a linear trend with unit slope for *CM* and *OC_A*, suggesting that uncertainty on model parameters affect variance and skewness of outputs in a similar way. Otherwise, considering *OC_G* we note that the influence of model parameters decreases for increasing order of the (statistical) moment of the output distribution, p_7 being an exception to this behavior.

5 Conclusions

This study compares a set of Global Sensitivity Analysis (GSA) approaches to evaluate the impact of conceptual geological model and parametric uncertainty on groundwater flow features in a three-dimensional large scale groundwater system. We document that the joint use of multiple sensitivity indices, each providing a particular insight to a given aspect of sensitivity, yields a comprehensive depiction of the model responses. In this sense, one minimizes the risk of classifying as unimportant some parameters which might have a non-negligible impact on selected features of the output of interest.

Our work leads to the following major conclusions.

1. Albeit being based on differing metrics and concepts, the three GSA approaches analyzed lead to similar and (generally) consistent rankings of parameters which are influential to the target model outcomes at the set of investigated locations. Otherwise, the choice of the conceptual model employed to characterize the lithological reconstruction of the system affects the degree of influence that uncertain parameters can have on modeling results.
2. When considering the overall behavior of model responses across the set of observation points, all GSA indices suggest that geomaterials constituting a relatively modest

fraction of the aquifer (~10÷15%) are influential to hydraulic heads only if they are associated with large conductivities. Otherwise (i.e., if their conductivity has a low to intermediate value), these geomaterials are not influential in any of the geological models considered.

3. The impact of very low conductivity geomaterials (such as those associated with facies 1 in Table 1) depends on the conceptual model adopted even when their volumetric fraction is significant (~30%). These geomaterials do not influence the variability of hydraulic heads computed through the *OC_A* model (Overlapping Continuum scheme associated with arithmetic averaging of geomaterial conductivities). Otherwise, they are seen to be remarkably influential for the *CM* (Composite Medium) model and the *OC_G* (Overlapping Continuum scheme associated with geometric averaging of geomaterial conductivities) model.
4. Uncertainty in the Neumann boundary condition plays only a minor role with respect to the Dirichlet boundary condition, which strongly controls variability of hydraulic head, in the *CM* and *OC_A* models. The opposite behavior is observed for the *OC_G* approach.
5. The moment-based indices AMAE, AMAV, and AMAγ (which quantify the impact of model parameters on the mean, variance, and skewness of the pdf of model outputs, respectively) suggest that input parameters which are evaluated as most influential affect in a similar way mean, variance and skewness of hydraulic heads for the *CM* and *OC_A* approaches. When considering the *OC_G* conceptualization, we note that the most influential parameters (i.e., the largest/smallest geomaterial conductivities, and Neumann boundary conditions) affects the mean of hydraulic heads more strongly than its variance or skewness.

6. The degree of symmetry of the pdf of hydraulic heads, as quantified by the skewness, depends on the considered conceptual model and varies across the domain. Conditioning on model parameters markedly affects the shape of the pdf of heads, whose degree of symmetry can strongly depend on conditioning parameter values.

Our results form the basis for future developments tied to efficient parameter estimation and uncertainty quantification in three ways: (i) parameters which have been identified as noninfluential to model outcomes (as expressed through their statistical moments of interest) can be neglected in a stochastic model calibration process and fixed to given values, (ii) quantification of differing impacts of model parameters on various (statistical) moments of model outputs can guide stochastic inverse modeling to identify posterior distribution of model parameters; and (iii) quantification of the way contributions to multiple statistical moments of model outputs are apportioned amongst diverse conceptual models and their parameters can be employed in a multimodel context. All of these topics are subject of current theoretical developments and analyses and will be explored in future studies.

Acknowledgements

The authors would like to thank the EU and MIUR for funding, in the frame of the collaborative international Consortium (WE-NEED) financed under the ERA-NET WaterWorks2014 Cofunded Call. This ERA-NET is an integral part of the 2015 Joint Activities developed by the Water Challenges for a Changing World Joint Programme Initiative (Water JPI).

References

Beretta, G.P., Francani V., Fumagalli L., 1992. Studio Idrogeologico della Provincia di Cremona (Hydrogeological study on Cremona Province), Pitagora Editrice, Bologna.

Borgonovo, E., Castaings, W., Tarantola, S., 2011. Moment independent importance measures: new results and analytical test cases. Risk Anal. 31, 404–428. https://doi.org/10.1111/j.1539-6924.2010.01519.x.

Box, G.E.P., Draper, N.R., 1987. Empirical model-building and response surfaces. Oxford, England: John Wiley & Sons.

Dai, H., Ye, M., Walker, A.P., Chen, X., 2017. A new process sensitivity index to identify important system processes under process model and parametric uncertainty. Water Resour. Res. 53(4), 3476-3490. https://doi.org/10.1002/2016WR019715.

Campolongo, F., Cariboni, J., Saltelli, A., 2007. An effective screening design for sensitivity analysis of large models. Environ. Model. Softw. 22, 1509-18. https://doi.org/10.1016/j.envsoft.2006.10.004.

Ceriotti, G., Guadagnini, L., Porta, G., Guadagnini, A., 2018. Local and global sensitivity analysis of Cr(VI) geogenic leakage under uncertain environmental conditions. Water Resour. Res. 54, 1-18. https://doi.org/10.1029/2018WR022857.

Chen, M., Izady, A., Abdalla, O.A., Amerjeed, M., 2018. A surrogate-based sensitivity quantification and Bayesian inversion of a regional groundwater flow model. J. Hydrol. 557, 826-837. https://doi.org/10.1016/j.jhydrol.2017.12.071.

Dell'Oca, A., Riva, M., Guadagnini, A., 2017. Moment-based metrics for global sensitivity analysis of hydrological systems. Hydrol. Earth Syst. Sci. 21, 6219-6234. https://doi.org/10.5194/hess-21-6219-2017.

Deman, G., Kerrou, J., Benabderrahmane, H., Perrochet, P., 2015. Sensitivity analysis of groundwater lifetime expectancy to hydro-dispersive parameters: The case of ANDRA Meuse/Haute-Marne site. Reliab. Eng. Syst. Safe. 134, 276-286. https://doi.org/10.1016/j.ress.2014.08.005.

Fajraoui, N., Ramasomanana, F., Younes, A., Mara, T.A., Ackerer, P., Guadagnini, A., 2011. Use of global sensitivity analysis and polynomial chaos expansion for interpretation of nonreactive transport experiments in laboratory-scale porous media. Water Resour. Res. 47, W02521. https://dx.doi.org/10.1029/2010WR009639.

Fajraoui, N., Mara, T. A., Younes, A., Bouhlila, R., 2012. Reactive transport parameter estimation and global sensitivity analysis using sparse polynomial chaos expansion. Water Air Soil Poll. 223(7), 4183-4197. https://doi.org/10.1007/s11270-012-1183-8.

Feil, B., Kucherenko, S., Shah, N., 2009. Comparison of Monte Carlo and Quasi Monte Carlo sampling methods in high dimensional model representation. In 2009 first international conference on advances in system simulation (pp. 12-17). New York, NY: IEEE. https://doi.org/10.1109/SIMUL.2009.34

Formaggia, L., Guadagnini, A., Imperiali, I., Lever, V., Porta, G., Riva, M., Scotti, A., Tamellini, L., 2013. Global sensitivity analysis through polynomial chaos expansion of a basin-scale geochemical compaction model. Computat. Geosci. 17, 25-42. https://doi.org/10.1007/s10596-012-9311-5.

Ghanem, R.G., Spanos, P.D., 1991. Stochastic Finite Elements: A Spectral Approach, Springer, N. Y.

Guadagnini, L., Guadagnini, A., Tartakovsky, D.M., 2004. Probabilistic reconstruction of geologic facies. J. Hydrol. 294, 57-67. https://doi.org/10.1016/j.jhydrol.2004.02.007.

Harbaugh, A.W., 2005. MODFLOW-2005. The U.S. Geological Survey Modular Ground-Water Model - the Ground-Water Flow Process. U.S. Geological Survey Techniques and Methods 6-A16.

Hutcheson, R.S., McAdams, D.A., 2010. A hybrid sensitivity analysis for use in early design. J. Mech. Des. 132(11), 111007-111007-10. https://doi.org/10.1115/1.4001408.

Isaaks, E.H., Srivastava, R.M., 1990. An Introduction to Applied Geostatistics. Oxford Univ. Press, New York.

Kerrou, J., Deman, G., Tacher, L., Benabderrahmane, H., Perrochet, P., 2017. Numerical and polynomial modelling to assess environmental and hydraulic impacts of the future geological radwaste repository in Meuse site (France). Environ. Modell. Softw. 97, 157-170. https://dx.doi.org/10.1016/j.envsoft.2017.07.018.

Laloy, E., Rogiers, B., Vrugt, J.A., Mallants, D., Jacques, D., 2013. Efficient posterior exploration of a high-dimensional groundwater model from two-stage Markov chain Monte Carlo simulation and polynomial chaos expansion. Water Resour. Res. 49, 2664–2682. https://dx.doi.org/10.1002/wrcr.20226.

Le Maître, O., Knio, O., 2010. Spectral methods for uncertainty quantification. Scientific Computation, Springer, Heidelberg, Germany. https://doi.org/10.1007/978-90-481-3520-2_1.

Liu, H., Sudjianto, A., Chen, W., 2006. Relative entropy based method for probabilistic sensitivity analysis in engineering design. J. Mech. Des. 128, 326-336. https://doi.org/10.1115/1.2159025.

Maina, F.Z., Guadagnini, A., 2018. Uncertainty quantification and global sensitivity analysis of subsurface flow parameters to gravimetric variations during pumping tests in unconfined aquifers. Water Resour. Res. 54, 501-518. https://doi.org/10.1002/2017WR021655.

Maione, U., Paoletti, A., Grezzi, G., 1991. Studio di gestione coordinata delle acque di superficie e di falda nel territorio compreso fra i fiumi Adda e Oglio e delimitato dalle Prealpi e dalla linea settentrionale di affioramento dei fontanili. (Study on surface and subsurface water management in the area between the Adda and Oglio river, the Prealpi line and the springs line).

Malaguerra, F., Albrechtsen, H.J., Binning, P.J., 2013. Assessment of the contamination of drinking water supply wells by pesticides from surface water resources using a finite element reactive transport model and global sensitivity analysis techniques. J. Hydrol. 476, 321-31. https://doi.org/10.1016/j.jhydrol.2012.11.010.

Morris, M.D., 1991. Factorial sampling plans for preliminary computational experiments. Technometrics 33, 161-174. https://dx.doi.org/10.1080/00401706.1991.10484804.

Pianosi, F., Beven, K., Freer, J.W., Hall, J., Rougier, J., Stephenson, D.B., Wagener, T., 2016. Sensitivity analysis of environmental models: a systematic review with practical workflow. Environ. Modelling Softw. 79, 214-232. https://doi.org/10.1016/j.envsoft.2016.02.008.

Pianosi, F., Wagener, T., 2015. A simple and efficient method for global sensitivity analysis based on cumulative distribution functions. Environ. Modell. Softw, 67, 1-11. https://doi.org/10.1016/j.envsoft.2015.01.004.

Rajabi, M.M., Ataie-Ashtiani, B., Simmons, C.T., 2015. Polynomial chaos expansions for uncertainty propagation and moment independent sensitivity analysis of seawater intrusion simulations. J. Hydrol. 520, 101-122. https://doi.org/10.1016/j.jhydrol.2014.11.020.

Rajabi, M.M., Ketabchi, 2017. Uncertainty-based simulation-optimization using Gaussian process emulation: Application to coastal groundwater management. J. Hydrol. 555, 518-534. https://doi.org/10.1016/j.jhydrol.2017.10.041.

Rametta, D., 2008. Interazione tra reticolo idrografico superficiale e acquifero sotterraneo nella modellistica idrologica distribuita (Study on surface-subsurface water interaction by means of a distribute model), Master Thesis, Politecnico di Milano, Milano.

Regione Emilia-Romagna, ENI-AGIP, 1998. Riserve idriche sotterranee della Regione Emilia-Romagna, S.EL.CA., Firenze.

Regione Lombardia, ENI-AGIP, 2002. Geologia degli acquiferi padani della Regione Lombardia, S.EL.CA., Firenze.

Razavi, S., Gupta, H.V., 2015. What do we mean by sensitivity analysis? The need for comprehensive characterization of ''global'' sensitivity in Earth and Environmental systems models. Water Resour. Res. 51, 3070-3092. https://doi.org/10.1002/2014WR016527.

Saltelli, A., Ratto, M., Tarantola, S., Campolongo, F., 2005. Sensitivity analysis for chemical models. Chem. Rev. 105(7), 2811-2827. https://doi.org/10.1021/cr040659d.

Sobol, I.M., 1993. Sensitivity estimates for nonlinear mathematical models. Math. Modeling. Comput. 1, 407-414.

Sobol, I. M., 2001. Global sensitivity indices for nonlinear mathematical models and their Monte Carlo estimates. Math. Comput. Simulat. 55(1–3), 271-280. https://doi.org/10.1016/S0378-4754(00)00270-6.

Sochala, P., Le Maître, O.P., 2013. Polynomial chaos expansion for subsurface flows with uncertain soil parameters. Adv. Water Resour. 62, 139-154. https://dx.doi.org/10.1016/j.advwatres.2013.10.003.

Song, X., Zhang, J., Zhan, C., Xuan, Y., Ye, M., Xu, C., 2015. Global sensitivity analysis in hydrological modeling: Review of concepts, methods, theoretical framework, and applications. J. Hydrol. 523, 739-757. https://doi.org/10.1016/j.jhydrol.2015.02.013.

Sudret, B., 2008. Global sensitivity analysis using polynomial chaos expansion. Reliab. Eng. Syst. Safe. 93(7), 964-979. https://doi.org/10.1016/i.ress.2007.04.002.

Winter, C.L., Tartakovsky, D.M., Guadagnini, A., 2003. Moment differential equations for flow in highly heterogeneous porous media. Surv. Geophys. 24(1), 81-106.

Xiu, D., Karniakidis, G.E., 2002. The Wiener-Askey polynomial chaos for stochastic differential equations. SIAM J. Sci. Comput. 24, 614-644. https://doi.org/10.1137/S1064827501387826.

TABLES

Table 1. List of the n_f = 5 facies (or geomaterial, classes) identified in the area, together with their volumetric fraction (f_i); ML estimates of indicator variogram range along the horizontal ($\hat{r}_h^i$) and vertical ($\hat{r}_v^i$) directions.

M_i	Description	f_i (%)	$\hat{r}_h^i$ (m)	$\hat{r}_v^i$ (m)
1	Clay and silt	36.77	467.4	17.1
2	Fine and silty sand	4.73	234.6	14.5
3	Gravel, sand and gravel	32.92	3835.2	17.5
4	Compact conglomerate, sandstone	14.94	2526.2	26.4
5	Fractured conglomerate	10.64	877.8	28.1

Table 2. Selected uncertain model inputs and associated intervals of variability, as defined by their lower ($p_i^{\min}$) and upper ($p_i^{\max}$) boundaries.

Parameter	Description	$p_i^{\min}$	$p_i^{\max}$
p_1 (m/s)	Conductivity of class 1, k_1	10^{-8}	10^{-5}
p_2 (m/s)	Conductivity of class 2, k_2	10^{-7}	10^{-4}
p_3 (m/s)	Conductivity of class 3, k_3	10^{-4}	10^{-2}
p_4 (m/s)	Conductivity of class 4, k_4	10^{-6}	10^{-3}
p_5 (m/s)	Conductivity of class 5, k_5	10^{-3}	10^{-1}
p_6 (m^3/s)	Neumann boundary condition*	4.83	14.47
p_7 (m)	Dirichlet boundary condition	0.0	3.0

*In terms of total flow rate imposed along the Northern domain boundary

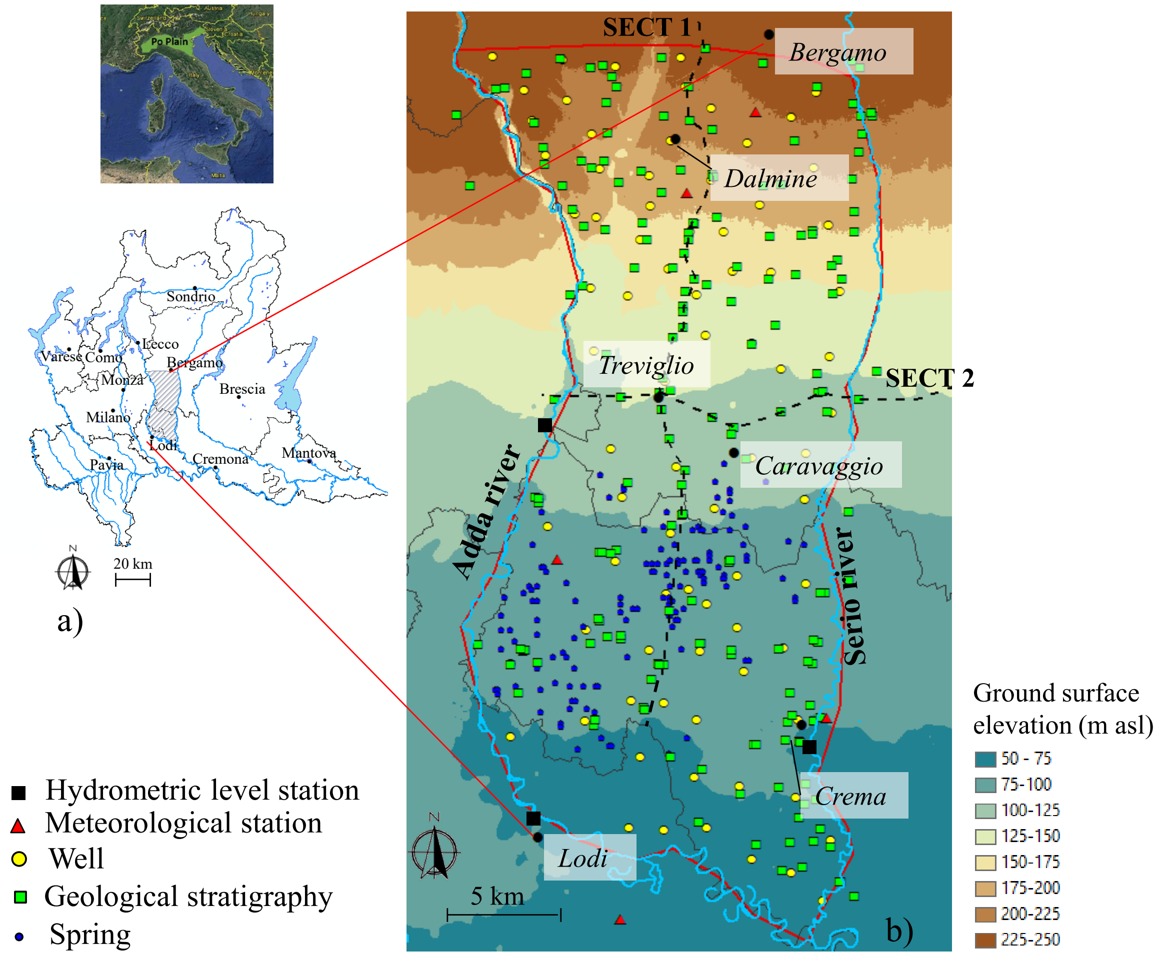

Fig. 1. Location of (a) the study area (shaded zone) within the Po Plain (Northern Italy) and (b) hydrometric and meteorological stations, pumping/monitoring wells, available geological stratigraphies and springs.

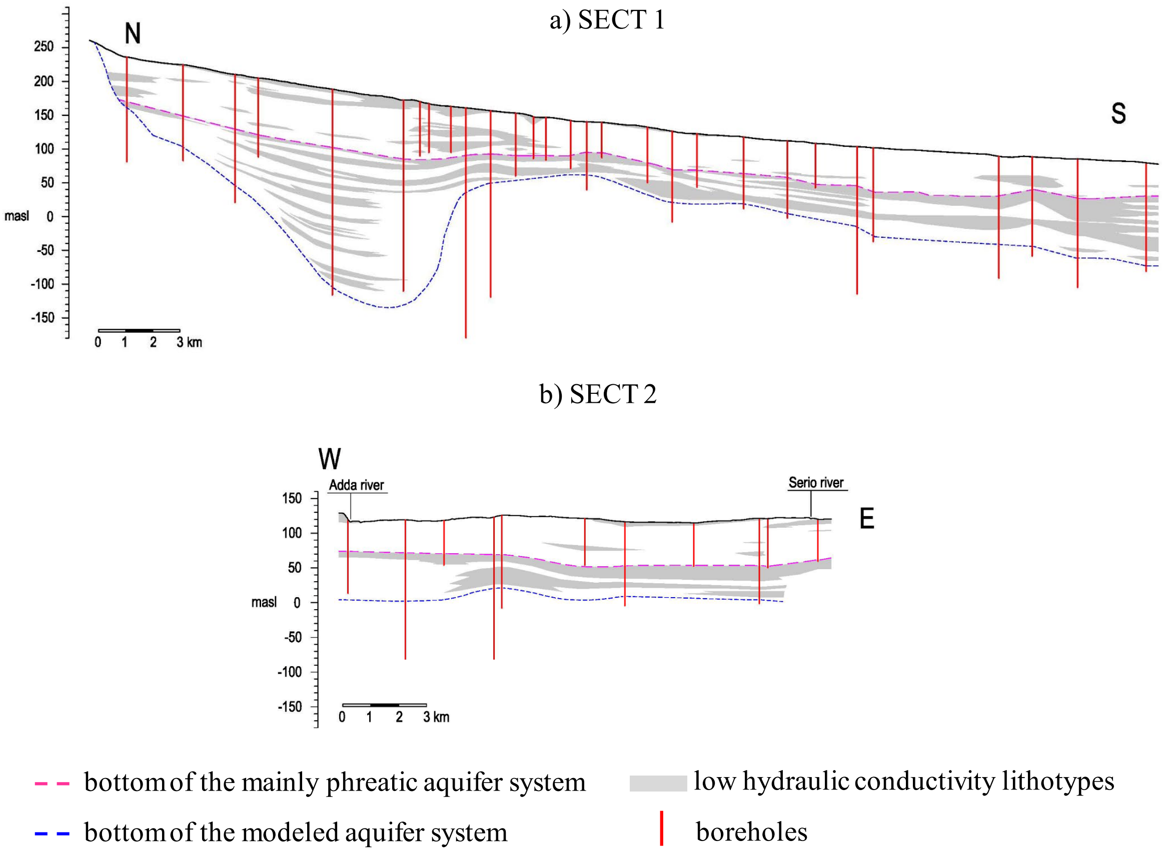

Fig. 2. Geological cross-sections (a) SECT 1 (North-South direction), and (b) SECT 2 (West-East direction), modified from Maione et al. (1991); see Fig. 1 for the location of the cross-sections.

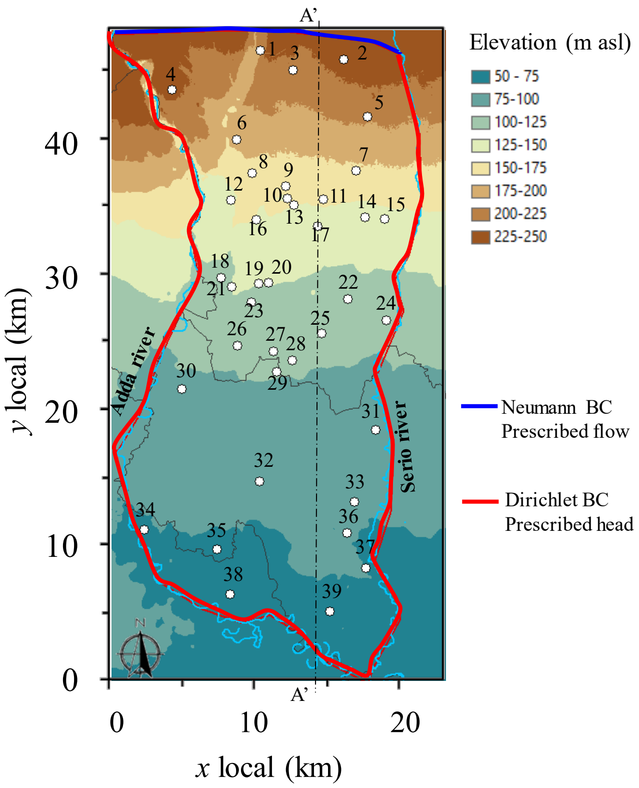

Fig. 3. Locations at which GSA metrics are evaluated and boundary conditions of the numerical model.

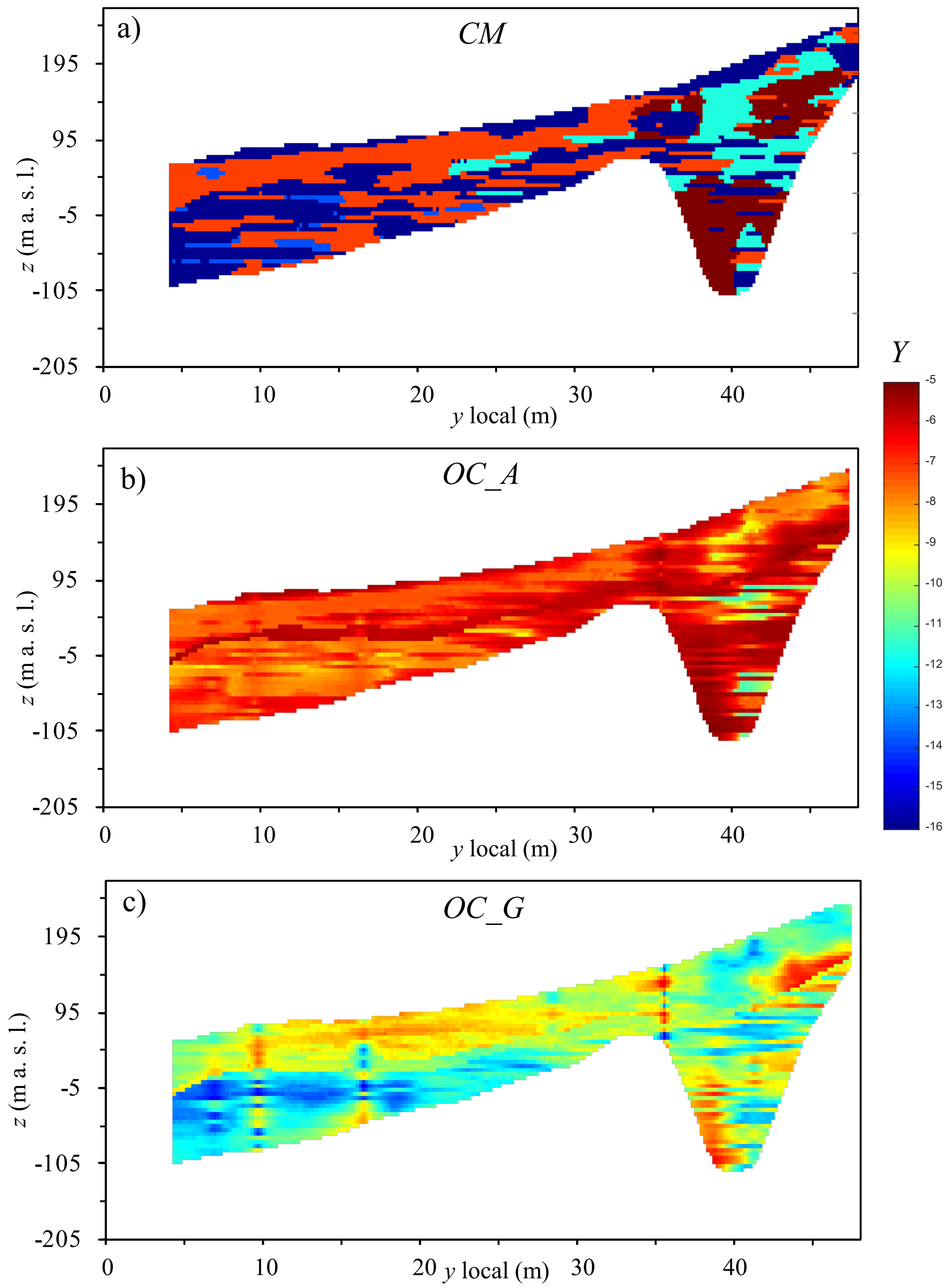

Fig. 4. Spatial distribution of the natural logarithm of hydraulic conductivity along longitudinal cross-section A'A' (see Fig. 3) for modeling strategies (a) *CM*, (b) *OC_A* and (c) *OC_G*. A vertical exaggeration factor of 50 is employed.

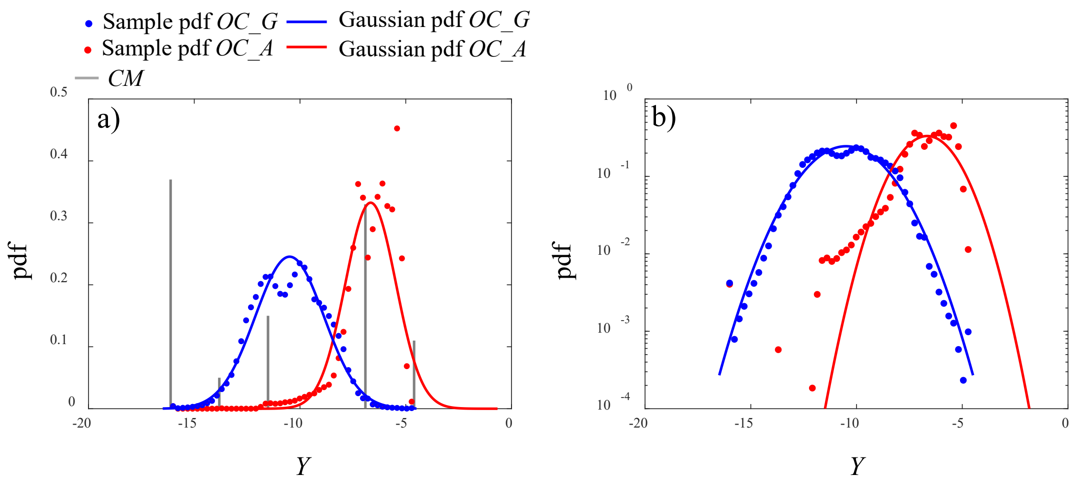

Fig. 5. Sample pdfs of Y for OC_A and OC_G on (a) natural and (b) semi logarithmic scales. Also shown for comparison are Gaussian distributions having the same mean and variance as the sample pdfs and (*ii*) the sample pdf evaluated for the *CM* model. Results correspond to the fields associated with the cross-sections depicted in Fig. 4.

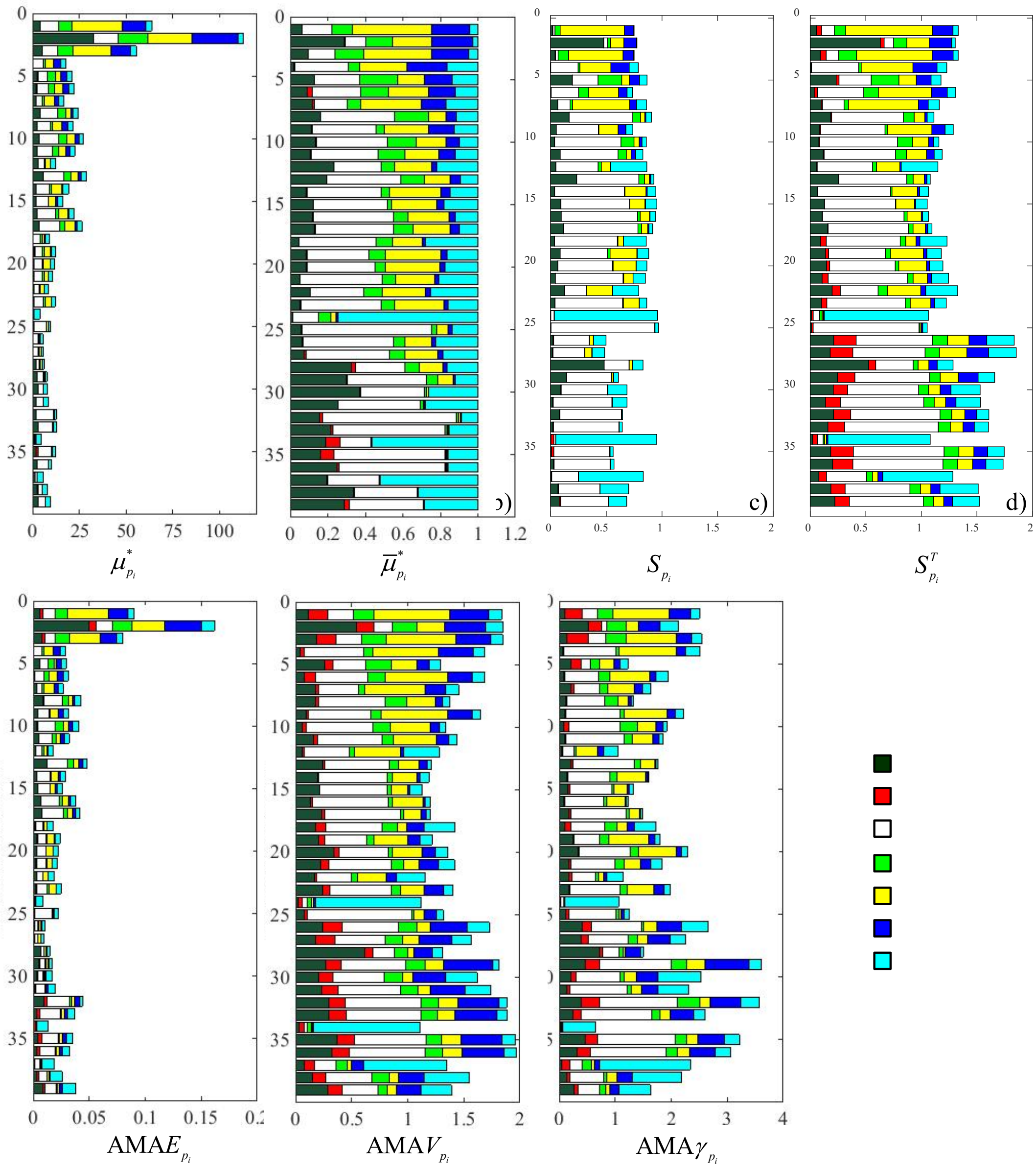

Fig. 6. *CM* approach. (a) Morris $\mu^*_{p_i}$, (b) Morris scaled $\overline{\mu}^*_{p_i}$, (c) principal Sobol' S_{p_i}, (d) total Sobol' $S^T_{p_i}$ (e) $\mathrm{AMA}E_{p_i}$, (f) $\mathrm{AMA}V_{p_i}$ and (g) $\mathrm{AMA}\gamma_{p_i}$ indices evaluated at the 39 locations depicted in Fig. 3.

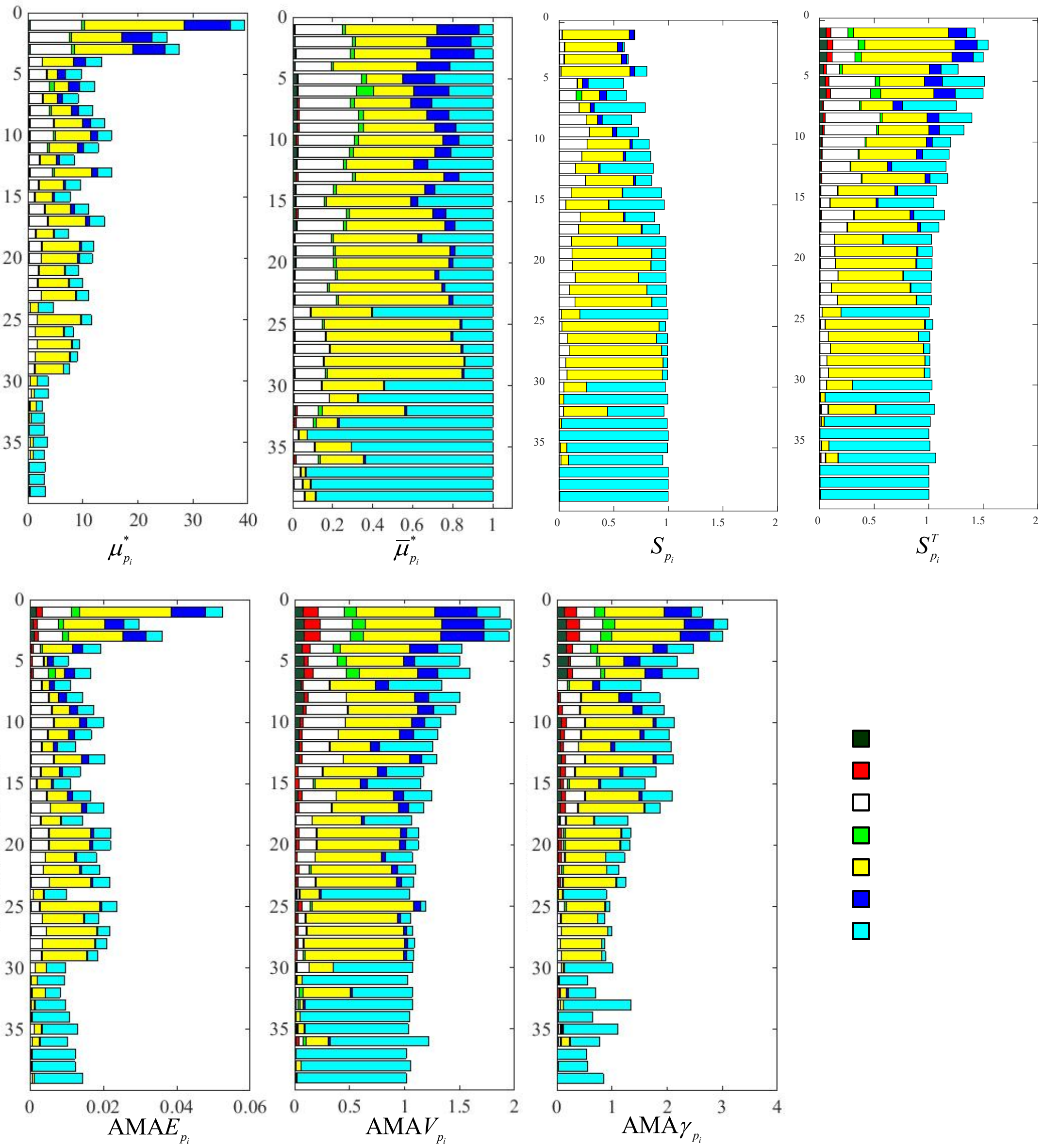

Fig. 7. *OC_A* approach. (a) Morris $\mu^*_{p_i}$, (b) Morris scaled $\bar{\mu}^*_{p_i}$, (c) principal Sobol' S_{p_i}, (d) total Sobol' $S^T_{p_i}$ (e) AMAE_{p_i}, (f) AMAV_{p_i} and (g) AMAγ_{p_i} indices evaluated at the 39 locations depicted in Fig. 3.

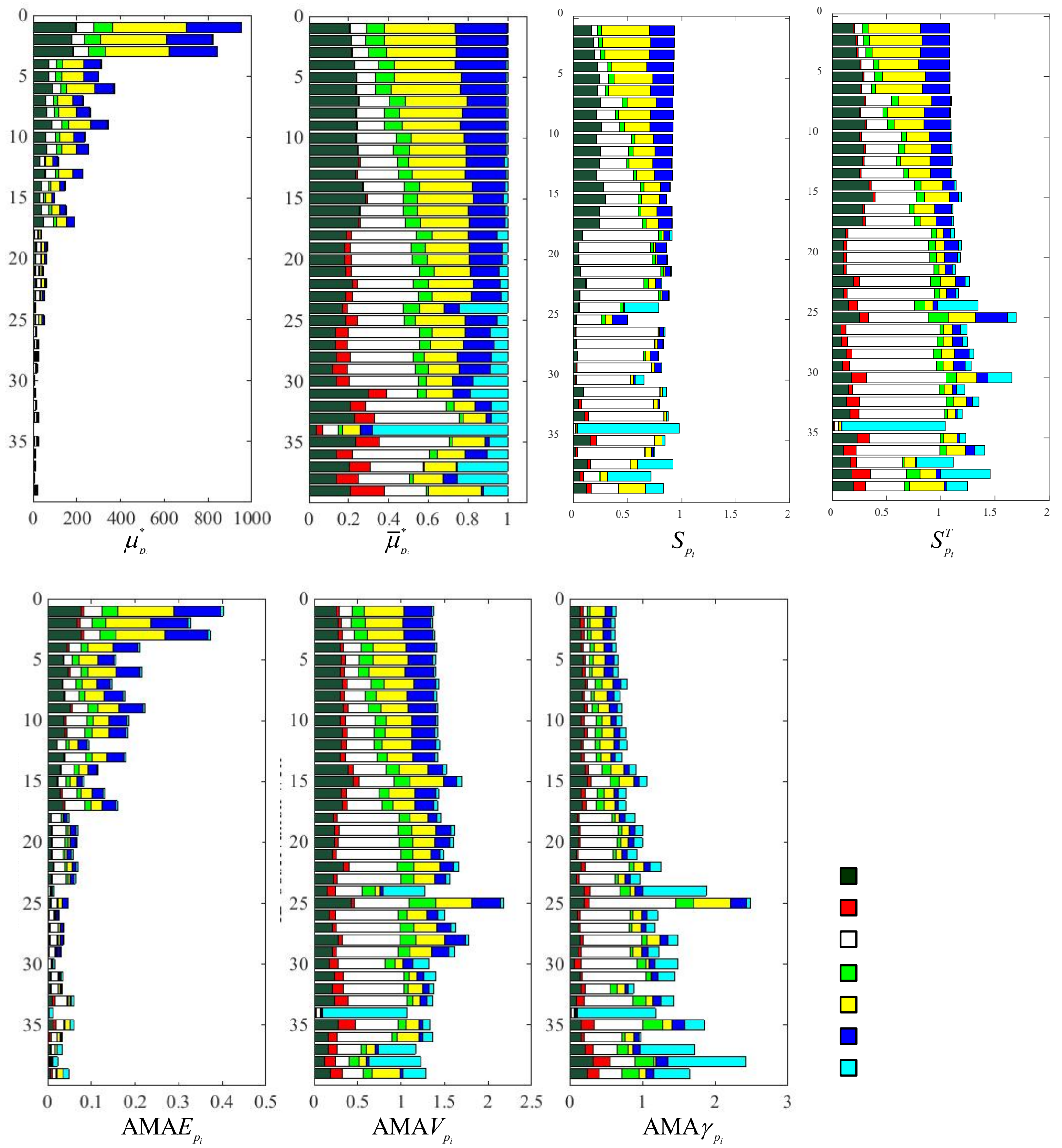

Fig. 8. *OC_G* approach. (a) Morris $\mu^*_{p_i}$, (b) Morris scaled $\overline{\mu}^*_{p_i}$, (c) principal Sobol' S_{p_i}, (d) total Sobol' $S^T_{p_i}$ (e) AMAE_{p_i}, (f) AMAV_{p_i} and (g) AMAγ_{p_i} indices evaluated at the 39 locations depicted in Fig. 3.

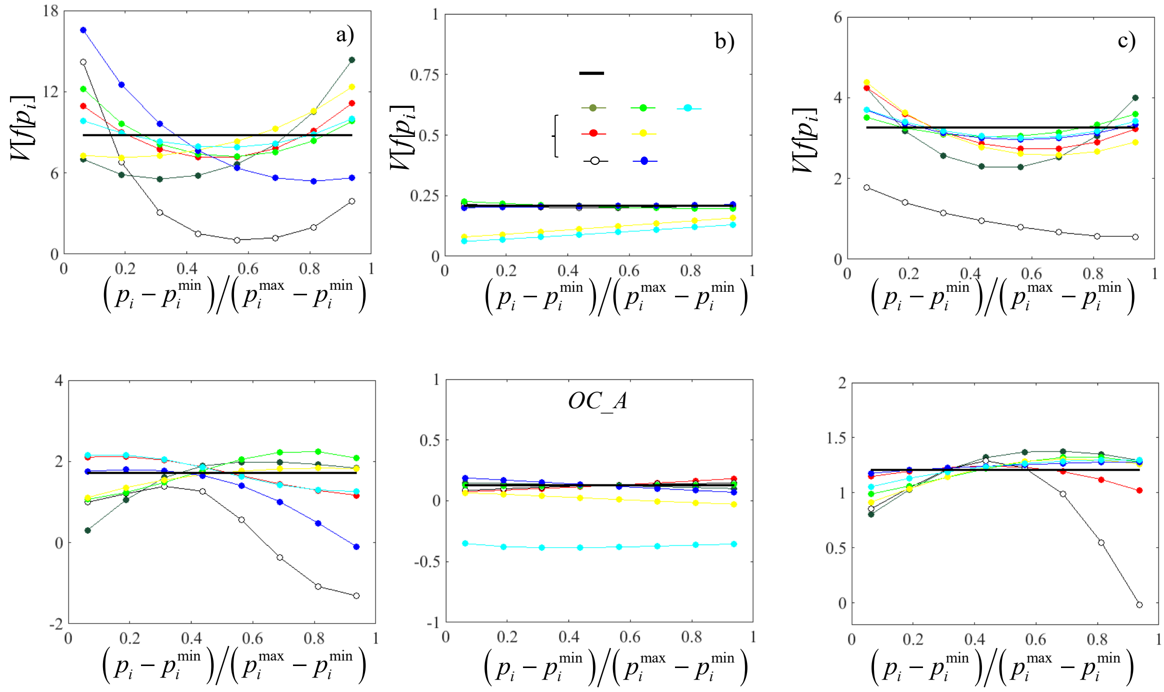

Fig. 9. Conditional (a-c) variance $V\left[f\middle|p_i\right]$ and (d-e) skewness $\gamma\left[f\middle|p_i\right]$ versus normalized p_i at a selected observation well (ID 32; see Fig. 3) for the conceptual models considered. The corresponding unconditional moments (horizontal black lines) are also shown.

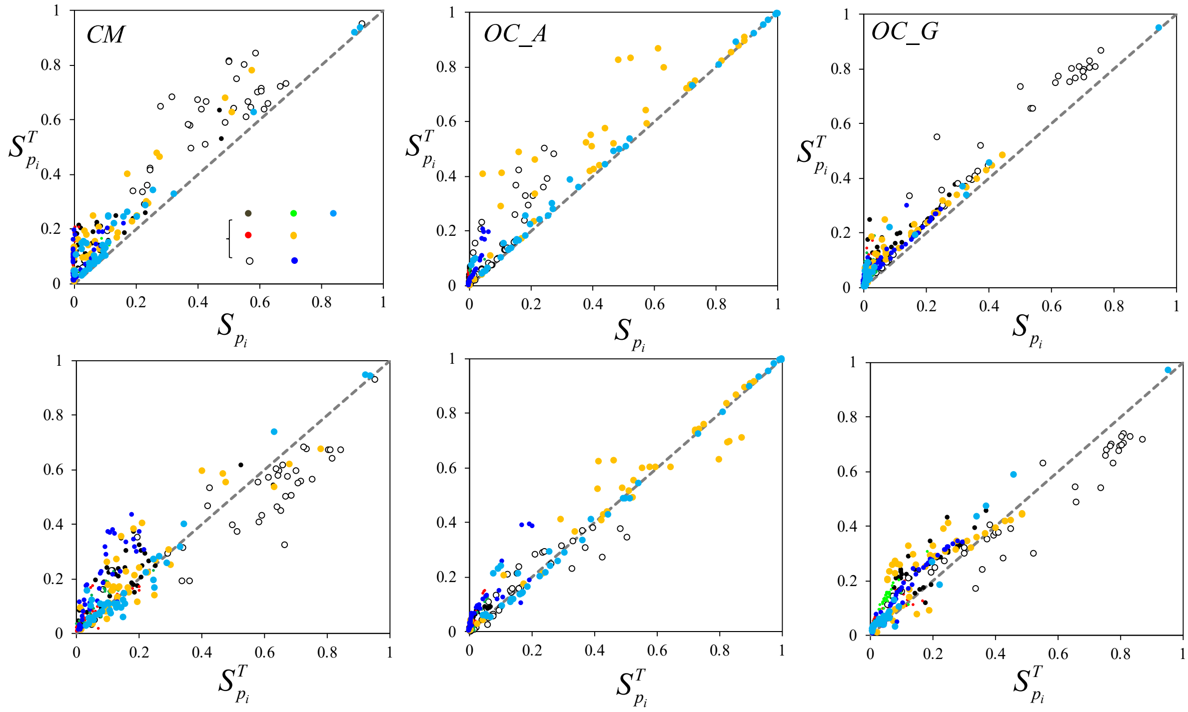

Fig. 10. Scatterplots of $S^T_{p_i}$ versus S_{p_i} (a-c) and $AMAV_{p_i}$ versus $S^T_{p_i}$ (d-f) at all 39 target locations for the conceptual models considered.

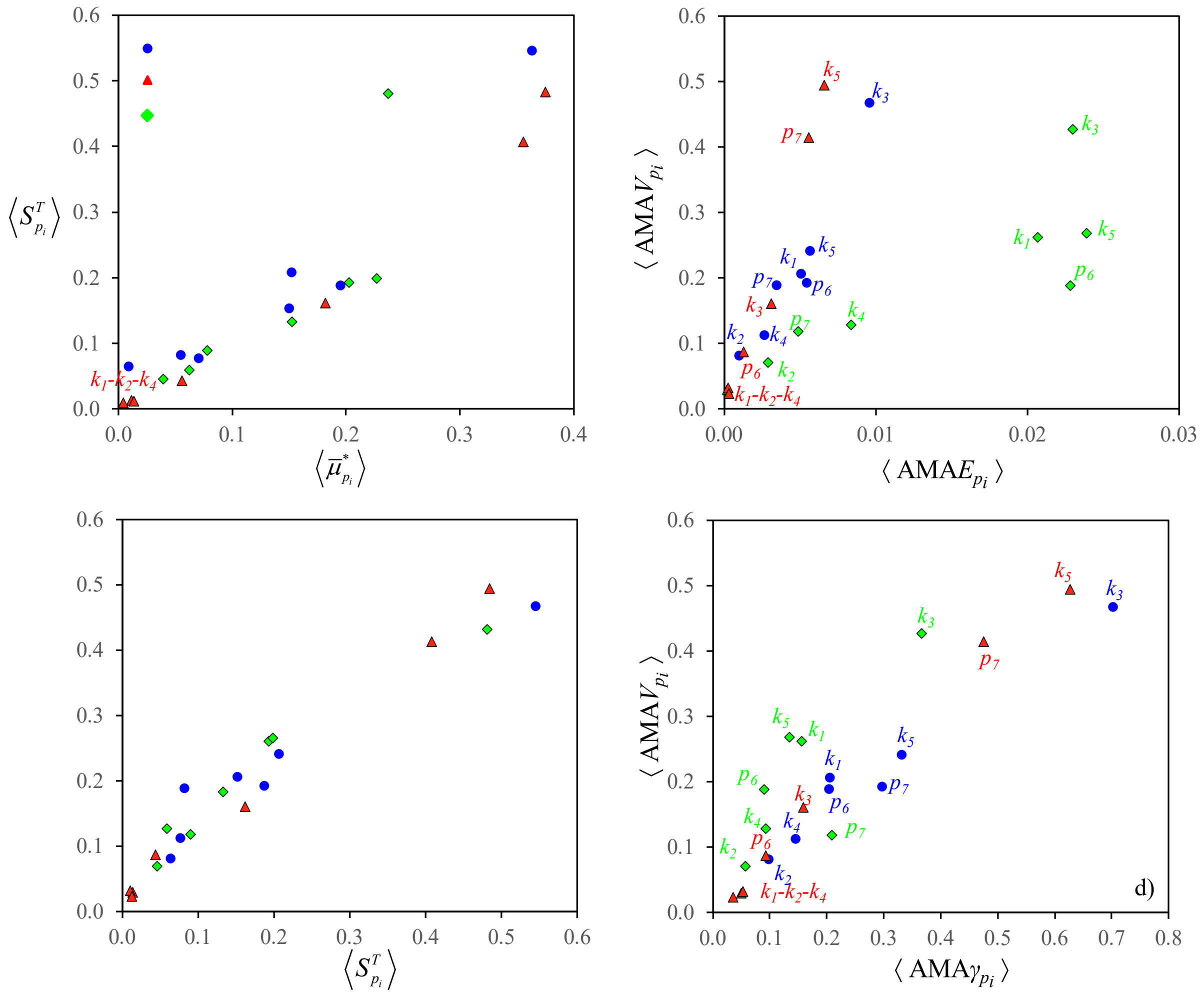

Fig. 11. Scatterplots of sensitivity indices averaged across all 39 target locations. (a) averaged total Sobol indices $\langle S_i^T \rangle$ versus averaged scaled Morris Index $\langle \bar{\mu}_i^* \rangle$; (b) averaged $\mathrm{AMA}V_{p_i}$ indices, $\langle \mathrm{AMA}V_{p_i} \rangle$ versus averaged $\mathrm{AMA}E_{p_i}$ indices, $\langle \mathrm{AMA}E_{p_i} \rangle$; (c) $\langle \mathrm{AMA}V_{p_i} \rangle$ versus $\langle S_i^T \rangle$; (d) $\langle \mathrm{AMA}V_{p_i} \rangle$ versus averaged $\mathrm{AMA}\gamma_{p_i}$ indices, $\langle \mathrm{AMA}\gamma_{p_i} \rangle$. Blue circles, red triangles, and green diamonds correspond to results obtained via the *CM*, *OC_A* and *OC_G* conceptual models, respectively.